Time-dependent forecast of large earthquakes from physics-informed probabilistic approach

This manuscript has been submitted for publication in NATURE COMMUNICATIONS. Please note that, despite having undergone peer-review, the manuscript has yet to be formally accepted for publication.

Sylvain Michel[1,2,3*†], Diego Molina-Ormazabal[4†], Jean-Paul Ampuero[1], Romain Jolivet[3,5], Andres Tassara[6]

[1]Université Côte d'Azur, Observatoire de la Côte d'Azur, IRD, CNRS, Géoazur, Valbonne, France.
[2]Sorbonne Université, CNRS-INSU, Institut des Sciences de la Terre Paris, ISTeP UMR 7193, Paris, France.
[3]Laboratoire de Géologie, Département de Géosciences, Ecole Normale Supérieure, PSL Université, CNRS UMR 8538, Paris, France.
[4]Université Grenoble Alpes, Univ. Savoie Mont Blanc, CNRS, IRD, Univ. Gustave Eiffel, ISTerre, Grenoble, France.
[5]Institut Universitaire de France, 1 rue Descartes, 75006 Paris, France.
[6]Departamento Ciencias de la Tierra, Facultad de Ciencias Químicas, Universidad de Concepción.

*Corresponding author(s). E-mail(s): Sylvain.MICHEL@geoazur.unice.fr;
†These authors contributed equally to this work.

Abstract

The elastic energy that fuels large earthquakes accumulates heterogeneously along faults, resulting in complex earthquake occurrence patterns. Although earthquake cycle simulations help capture such complexity in seismic hazard models, their high computational cost prevents widespread use and uncertainty quantification. Here, we propose a physics-based probabilistic method to forecast the timing and magnitude of large earthquakes. The method combines fracture mechanics theory and observational constraints on seismic coupling,

historical seismicity and fracture energy to forecast the arrest locations of long ruptures that have saturated the seismogenic depth. We apply this approach to estimate the time-dependent probability of earthquakes exceeding M8.5 across the entire Chilean subduction zone. Sensitivity analysis shows the most critical model parameter relates to the scaling between fracture energy and slip. We constrain the model parameters by matching the time between mega-earthquakes on the Valdivia segment, validate the constrained model based on the seismicity of other segments, then apply it prospectively over the whole Chile megathrust. Our results highlight how earthquake potential on a given megathrust segment can be altered by earthquakes on neighboring segments, which reduce the energy available for multi-segment ruptures. The proposed physics-informed framework constitutes a new approach for time-dependent seismic hazard analysis on large faults.

1 Introduction

Estimating the frequency and size of future earthquakes is critical for seismic hazard assessment. This requires defining not only where and when earthquakes can start, but also where their ruptures will stop, which is not trivial on very long faults with multiple segments that might rupture simultaneously [1].

Current time-dependent models used in seismic hazard assessment are a statistical description of the expected time of the next earthquake depending on the time elapsed since the previous one [2]. Point process models are often applied on individual fault segments, assumed disconnected and hosting characteristic earthquakes of a certain size [e.g. 3, 4]. Their controlling parameters, including the mean recurrence time and the deviation from periodic recurrence, can be constrained by past seismicity [5–7]. However, due to their oversimplified assumptions, such models poorly describe sequences of earthquakes with rupture extents that might breach segment barriers and overlap [2, 8].

One important factor controlling the propagation and final size of earthquakes is the elastic energy available around the fault [9], which is generally space- and time-dependent due to tectonic stress accumulation, non-planar fault geometry, and the

continuous stress redistribution by seismic activity and fault creep. Interseismic coupling maps inferred from geodetic observations [10, 11] allow to identify areas that accumulate slip deficit, thus elastic energy, and can potentially host future large earthquakes [12, 13]. Although slip deficit informs about the maximum slip that future earthquakes can release at any given point on the fault, it does not directly inform about where a rupture will stop, hence its final magnitude. Coulomb stress change analyses of interactions between fault segments [e.g. 14, 15] have been used to assess whether a rupture can jump from one segment to another, but they do not allow to evaluate whether a jumping rupture will propagate further along the receiving segment.

Incorporating the physics of earthquake rupture dynamics is a promising avenue to advance earthquake hazard assessment [16, 17]. A recent extension of fracture mechanics theory to elongated ruptures (length $>$ width), relevant for large earthquakes that saturate the seismogenic width, provides a framework to evaluate whether a section of a fault tends to hinder or fuel rupture propagation [9]. Important implications of this theory were discussed for a segment of the Chilean subduction zone [18] and for a crustal fault system in China [19] using coupling maps to constrain the elastic energy available along the fault. Here, we take a major step towards integrating this theoretical framework into seismic hazard analysis by developing a method that generates millions of earthquake scenarios, enabling the probabilistic assessment of time-dependent earthquake potential across the entire length of a fault with exhaustive uncertainty quantification.

In this study, we apply this extension of fracture mechanics to assess the rupture potential of the entire Chilean subduction megathrust. Its historical earthquake record spans 500 hundred years (Fig. 1a) [e.g. 20–24], its paleo-seismological record at least two millennia [e.g. 25, 26], and available interseismic coupling maps cover the entire region (Fig. 1b) [e.g. 12, 20, 27–29]). The available dataset is therefore adequate to

calibrate and validate the framework. Additionally, coupling ratio and seismogenic depth vary along strike allowing us to examine the influence of the segmentation of the seismogenic megathrust on the earthquake potential (Fig. 1c).

We evaluate the sensitivity of our framework to parameter uncertainties, revealing that the key parameter is the coefficient that controls the scaling of fracture energy with slip. We constrain the model parameters by confronting our model to the observed earthquake record of the well-studied Valdivia segment, which hosted the giant M9.5 1960 earthquake. Using this constrained model, we evaluate the spatial and temporal evolution of the probability of occurrence of an earthquake of a certain size along the whole Chile subduction, for retrospective validation and prospective forecasting. These results illustrate how a physics-based model can inform probabilities of earthquake occurrence, hence seismic hazard studies, especially in current seismic gaps where large earthquakes are overdue [30–32].

2 Determining the rupture extent of elongated earthquakes

Once a rupture has saturated the seismogenic width of a fault (W), it can only continue growing by propagating horizontally. In the fracture mechanics theory of such elongated ruptures [9, 18], the propagation and arrest of a rupture are controlled by the ratio G_c/G_0 between fracture energy G_c and elastic energy release rate G_0. A fault section hinders rupture propagation if it satisfies $G_c/G_0 > 1$; otherwise, it fuels the rupture. This energy ratio varies along the fault and evolves through the interseismic period. Given the spatial distribution of G_c/G_0 along a fault, the rupture arrest locations are determined by a criterion based on a "rupture potential", Φ, defined at any

along-strike location L, relative to an arbitrary reference location, 0:

$$\Phi(L) = \int_0^L \frac{1 - G_c/G_0}{W} dL. \tag{1}$$

An elongated bilateral rupture starting at position L_0 will stop at the positions L_- and L_+ where the rupture potential is the same as that of the hypocentral region, i.e. where $\Phi(L_0) = \Phi(L_-) = \Phi(L_+)$, as illustrated in Fig. S6.

Our estimates of the energy ratio are constrained by the slip deficit derived from maps of interseismic coupling (χ). As a conservative approach, we assume that ruptures involve a coseismic slip D equal to the whole slip deficit accumulated at a time t since the last large event, $D = \chi V_{plate} t$, where V_{plate} is the long-term slip rate. At each location on the fault, the oldest known large event sets the onset time for our modeling (e.g., in Chile, 1575 for the Valdivia segment and 1995 for the Antofagasta segment; Fig. 1a).

For sub-shear ruptures, the elastic energy release rate is approximately [18]

$$G_0 \approx C(\theta, \nu) \left((1-\nu)^{-1} \cos^2\theta + \sin^2\theta \right) \ \mu (\chi V_{plate} t)^2 / W \tag{2}$$

where μ is the shear modulus, θ the rake angle, $C(\theta, \nu)$ a geometric factor of order 1 given by Eq. 3, and $\nu = 0.25$ the Poisson's ratio. The parameters involved in this equation are quite well constrained by geophysical observations in Chile (Methods), and only the coupling ratio χ and seismogenic width W are considered here to vary along-strike.

We relate fracture energy G_c to coseismic slip D using a compilation of estimates derived from laboratory experiments, geological measurements, seismological data, and numerical modeling [33] (Fig. S1). Since we focus on large megathrust earthquakes, we consider estimates obtained from seismological data for $D > 0.1$ m. We fit a scaling

law of the form $G_c \approx BD^n$, where G_c is in MJ.m^{-2} and D is in meters, yielding $B = 2.60$ and $n = 1.02$. The value of n is close to 1, consistent with models of dynamic rupture with off-fault inelastic dissipation [34, 35].

Using these local estimates of G_c and G_0 based on the slip deficit D accumulated since the last rupture, we evaluate the time- and space-dependent seismogenic potential. We assume earthquakes can nucleate anywhere on the seismogenic zone and, at a given time t, we examine a comprehensive set of earthquake scenarios spanning all possible hypocenter locations on the megathrust (Fig. S5). In each scenario, we consider a "saturating earthquake", i.e. one whose rupture has already grown enough to saturate the seismogenic zone, and use our model to predict where the rupture will stop and the final earthquake magnitude. In particular, for a given epicenter location, we compute the rupture potential $\Phi(L)$ along the fault and then use it to determine the rupture arrest points L_- and L_+ (e.g., Fig. S6). A more detailed description of the procedure is provided in the Method section. Owing to the small computational cost of our approach, we can thoroughly consider millions of earthquake scenarios at any given time, as needed for probabilistic analysis and uncertainty quantification.

3 Parameter Sensitivity Analysis

We evaluate how the uncertainties in model input parameters affect model results, by focusing on a key model outcome: the "critical time" T_c when a fault section reaches the condition $G_0 > G_c$ required to fuel rupture propagation. Since $G_c/G_0 \propto D^{n-2}$ with $n - 2 < 0$, the energy ratio decreases over time as slip deficit D accumulates, from very high values ($G_c/G_0 \gg 1$) soon after a large earthquake to values promoting rupture propagation ($G_c/G_0 < 1$) after a finite time T_c given by Eq. 4 (Methods). For a given distribution of model parameters (Fig. 2), characteristic of those constraining our model in Chile, we compute the corresponding distribution of T_c. This approach

allows us to evaluate the effect of the chosen parameter values on the transition time at a given position along the fault.

Two sensitivity analyses are performed: (1) we fix the value of one parameter and evaluate the effect of the uncertainties of the remaining ones (Fig. 2g); (2) we fix all parameters but one and evaluate the effect of the uncertainty of this single parameter (Fig. 2h). In the first analysis, the coefficient B of the scaling between fracture energy and slip is the only parameter that, if fixed, leads to a significant change in the probability density function (PDF) of T_c (Fig. 2g). In the second analysis, the PDF of T_c obtained when varying only B is very similar to the PDF obtained by varying all the parameters. Thus, the distribution of T_c is primarily controlled by the uncertainty on B, which in turn is likely due to the high uncertainties in estimates of Gc for natural earthquakes and their intrinsic variability [33]. The other parameters have a significantly smaller effect on T_c. For instance, for this example, varying B modulates T_c between ∼30 and 1610 yrs, while varying W modulates T_c between ∼200 and 280 yrs and varying θ has almost no impact.

Given the critical role of B, it is crucial to continue collecting and improving estimates of G_c and D for large earthquakes. Next, we show how to further constrain B using historical data.

4 Constraining the scaling relation between fracture energy and slip

To better constrain B, we confront the results of the time and space-dependent seismogenic potential model with the sequence of major earthquakes on the Valdivia segment in southern Chile (Fig. 1a). Paleo-seismological evidence indicates an earthquake recurrence time of 250-350 years during the last 2 millennia, with the latest major events being the 1960 M_w 9.5 event and a large megathrust earthquake in 1575

[25, 36]. Two other relatively large events occurred in 1737 and 1837, but likely ruptured only a limited portion of the segment [25]. The slip deficit accumulated since 1575 is consistent with the slip estimated for the 1960 earthquake (∼20-35 m; [37]).

At any given time after 1575, we use our model to test whether hypothetical saturating earthquakes that contain the 1960 Valdivia earthquake epicenter can propagate further and rupture the portion of the Valdivia segment south of latitude 38°S. This procedure allows to avoid using the portion of the Valdivia segment that overlaps with the Maule earthquake of 1751 as a constraint, as the lateral extent of this earthquake is uncertain. For the 1960 earthquake to occur in our model, the segment needs to be ready to break before this date. The subset of B values consistent with this constraint is shown in Fig. 3 (dark blue PDF). The result for all parameters is shown in Fig. S2. If we assume that the 1960 earthquake occurred immediately after the segment was ready, the subset of admissible B values is even tighter (light blue PDF; Fig. S2). This constrained PDF aligns well with the $G_c - D$ scaling data (gray histogram in Fig. 3) and its fit (Section 2; Fig. S1). This cross-validation comforts us that the range of B constrained by assuming the fault is ready exactly in 1960 is reasonable; therefore, we use it in the remainder of this study.

5 The seismogenic potential of the Chile subduction megathrust

We now assess the time- and space-dependent seismogenic potential along the whole Chile subduction zone. We account for the spatial variation and uncertainties of the parameters (Methods), focusing on scenarios consistent with the 1960 earthquake occurring immediately after the southern portion of the Valdivia segment is ready. This approach constrains the values of B explored as well as the other parameters in

a self-consistent way (Fig. S2). At each time, 19 million scenarios are evaluated, considering 915 potential initial rupture and nucleation positions and probing parameter uncertainties using 21,000 random samples (Fig. S5).

We first evaluate the PDF of the critical time T_c at each latitude (Fig. 4b) and find an overall consistency with the activity of the major segments of the Chilean subduction zone. Along the Valdivia segment, the mode of T_c (red line in Fig. 4b) falls slightly before the occurrence of the 1960 earthquake, by design of our calibration of model parameters. Along the Maule segment, the mode of T_c roughly matches the timing of the 2010 earthquake. Its spatial variation reflects changes in coupling, yielding larger T_c values (i.e. later readiness) in the northern part of the Maule segment, which may explain why the 2010 event did not extend further north. To the south, the low available potential energy due to the 1960 Valdivia earthquake contributes to hinder the southward propagation of the Maule earthquake.

Along the Valparaiso segment, when the 2015 Illapel earthquake broke the segment only partially, the model indicates that a full-segment rupture was most likely but partial-segment ruptures remained significantly probable. Along the Iquique segment, the 2014 earthquake occurs when the segment is not completely ready, which is consistent with the fact that the event saturated the seismogenic zone but did not propagate further. The rough timing constraints derived from T_c highlight that our model captures to first order relevant factors governing rupture propagation and timing in these segments. Other interpretations of the sequence of old earthquakes might lead to different results, as discussed in the Method section, which could be handled by accounting for uncertainties on paleo-seismic data in our approach.

Moving forward from the analysis of the critical time T_c, we evaluate whether saturating earthquakes can propagate further and become very large earthquakes. Considering the moment-area scaling law [38], saturating ruptures in Chile have a minimum magnitude $M_{SAT} \approx$ 8.0-8.3 (Methods). We hence consider our results for

events with magnitude above 8.3. We compute the probability $P_{M>X|SAT,t}$ that a fault location can participate in a saturating event that grows to a magnitude exceeding X, at time t (Methods). Fig. 4c shows the space-time evolution of $P_{M>8.5|SAT,t}$ while Fig. 4d shows the temporal evolution of its mean within each segment. This analysis reveals the influence of the interconnection between segments. If a fault segment were isolated from the rest of the fault, its $P_{M>8.5|SAT,t}$ would increase gradually (e.g. black dashed line in Fig. 4e). Because ruptures can break through segment boundaries, the evolution of the rupture potential of a segment influences the evolution of $P_{M>8.5|SAT,t}$ on other segments (Fig. 4d). For instance, along the Copiapo segment, $P_{M>8.5|SAT,t}$ decreases after the 1960 Valdivia, 2010 Maule and 2015 Illapel earthquakes because these events reduce the energy available in their segments, which in turn reduces the likelihood of multi-segment ruptures reaching the Copiapo segment. Furthermore, the increase in $P_{M>8.5|SAT,t}$ on the Copiapo segment at the beginning of the loading period (between 1906 and 1960) is faster than if the segment was isolated (see Fig. 4e). High values of $P_{M>8.5|SAT,t}$ initially concentrated at the southern border of the Copiapo segment gradually expand northward over time (Fig. 4c). This results from the progressive loading of the Valparaiso, Maule and Valdivia segments which increases the likelihood of a large earthquake initiating within these regions and propagating through the Copiapo segment.

6 Towards Efficient Physics-Based Seismic Hazard Assessment

While we do not attempt to predict the exact time and magnitude of the next large earthquake, our model provides a probabilistic forecast based on a physical and statistical approach that is consistent with the observed earthquake history. It specifically accounts for the spatial variability of energy along a fault due to differences in coupling and the timing of previous large earthquakes.

In particular, our approach yields the conditional probability $P_{M>X|SAT,t}$ of the occurrence of an earthquake above magnitude X at time t, provided that it has already developed into a saturating event. The probability of occurrence of an elongated earthquake above magnitude X is $P_{M>X \bigcap SAT} = P_{M>X|SAT,t} \times P_{SAT}$, where P_{SAT} is the inter-event time probability of saturating events since their last occurrence, evaluated over a specified time interval centered at time t. P_{SAT} depends on the rate of occurrence of saturating events and we propose in the Method section two alternative approaches to evaluate it.

Our model can incorporate possible dependencies of P_{SAT} on location along the fault and on time since the last large earthquake. For example, Fig. S3 shows P_{SAT}, $P_{M>X|SAT,t}$ and $P_{M>X \bigcap SAT}$ for a mean rate of saturating events of $1/90$ yrs^{-1}, assuming the occurrence of saturating events follows a random Poisson process.

The rate of occurrence of saturating events is a crucial model input to assess seismic hazard. If it is very low, the fault will remain unbroken until it is ready to host full-segment events, and ruptures will rarely stay at $M_w = M_{SAT}$, they will rather propagate into large events. Conversely, if the rate of saturating events is extremely high, the fault will rarely be ready to host large events, and magnitudes will remain close to M_{SAT}. Examples of these end-member behaviors might be the Cascadia [39] and Vanuatu [40] subduction zones, respectively. Thus, the rate of saturating events is expected to control the shape of the magnitude-frequency distribution of very large earthquakes.

Beyond the probabilities discussed above, our framework provides a generative model of earthquake scenarios for practical hazard assessment. This framework can be used to generate catalogs of large earthquakes, in particular their rupture location, rupture history and final slip distribution. These rupture scenarios can be readily combined with ground motion models to evaluate site-specific hazard and produce regional (time-dependent) hazard maps.

As a compromise to develop a computationally-efficient model, strong assumptions are made to simplify the complex and evolving behavior of natural faults. We assume that slip deficit accumulates over interseismic periods at a steady rate that is spatially prescribed by a coupling distribution inverted from recent (¡30 years) geodetic data. We also assume that this slip deficit is fully released by large earthquakes, ignoring static and viscoelastic stress transfer after each earthquake [41], the occurrence of slow slip events [42–44], and super-cycle behavior with coseismic slip undershooting or overshooting the slip deficit [45]. Moreover, the model does not currently consider non-planar fault geometry, frictional heterogeneities or other types of obstacles that could hinder the propagation of earthquakes [e.g. 46–49]. Last but not least, uncertainties in the occurrence time and rupture extent of old large earthquakes in the historical and paleoseismic records are substantial [22–24] and remain to be integrated in our model.

Although crucial, many of these limitations are partially accounted for by parameter uncertainties. Moreover, most of these biases and missing elements can be addressed through future research and each ingredient of the framework can be refined. Ongoing and continuous efforts to improve our knowledge of faults —in particular fracture energy, fault coupling and seismogenic width —and past earthquakes are critical for seismic hazard assessment. Applying the approach to other subduction zones would further constrain and test the model. Such efforts could lead, for instance, to establish relations between model parameters controlling fault behavior, in particular the energy scaling coefficient B, and observable physical properties along subduction zones, such as seafloor roughness, sediment thickness or seismic wave speeds. The approach could also be tested prospectively on Slow Slip Events [50], owing to their short recurrence times, and for which many earthquake cycles involving multiple megathrust segments have been recorded.

Our study demonstrates that combining a physics-based model with statistical analysis provides a quantitative framework to assess the seismogenic potential of subduction zones. The application to the Chile subduction zone highlights how fault interactions can modulate the seismogenic potential in space and time, offering a new perspective on space- and time-dependent seismic hazard assessment. The framework can reveal regions that are more susceptible to host large earthquakes, helping to establish hazard mitigation measurements in a more effective and organized manner. It could also potentially be used in early warning systems as prior information to forecast the final size of a rupture that has just saturated the seismogenic zone.

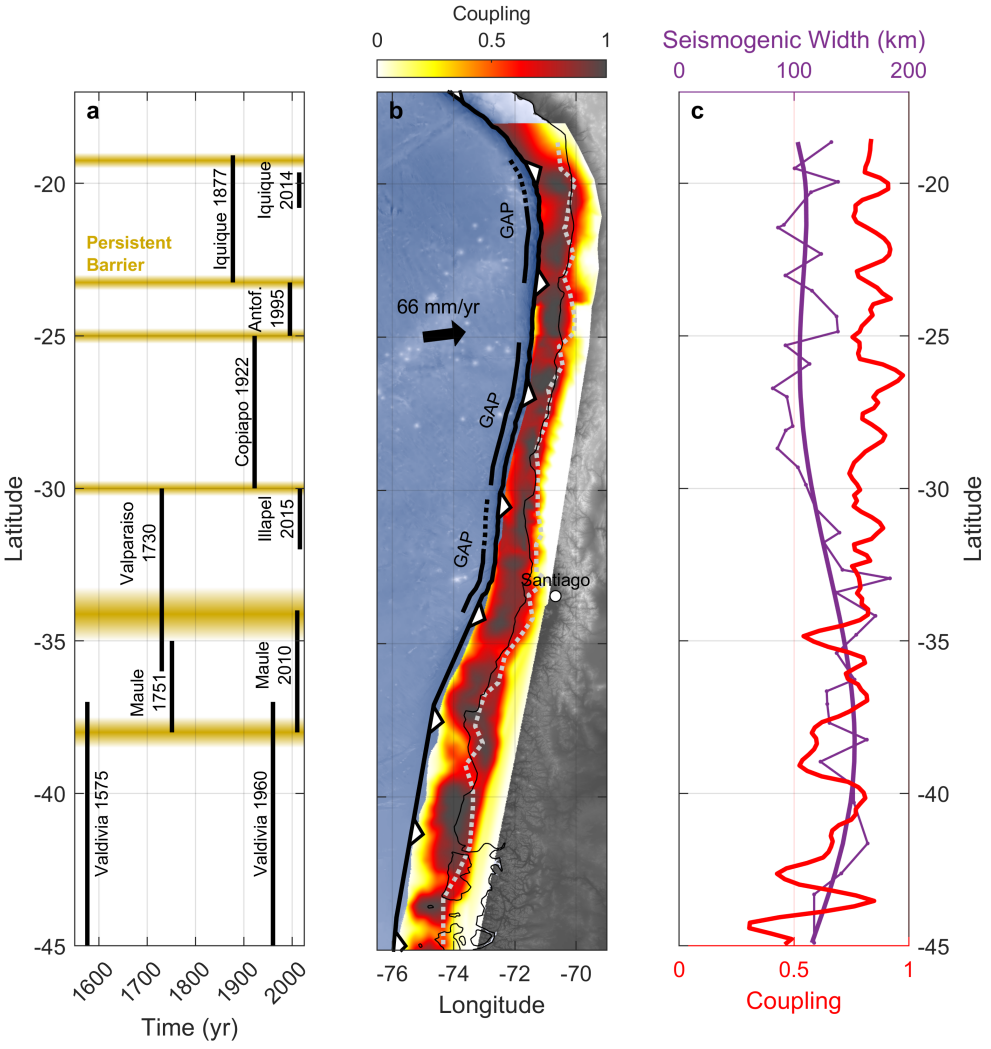

Fig. 1 Overview of the Chilean subduction zone. (a) Past seismicity and fault segmentation (modified from [20]). Rupture extent and occurrence time of historic earthquakes are indicated by black bars. Areas identified as persistent barriers to the propagation of earthquakes are shown in yellow. **(b)** Interseismic coupling along the Chilean subduction interface (yellow to brown shading, [12, 20, 27–29]), seismogenic depth estimated from seismicity distribution (light gray dotted curve) and current seismic gaps. Thin and thick black lines indicate the coast and the subduction trench, respectively. **(c)** Lateral distributions of seismogenic width (thick purple curve), its smoothed version (thin blue curve), and depth-averaged interseismic coupling (red curve).

322

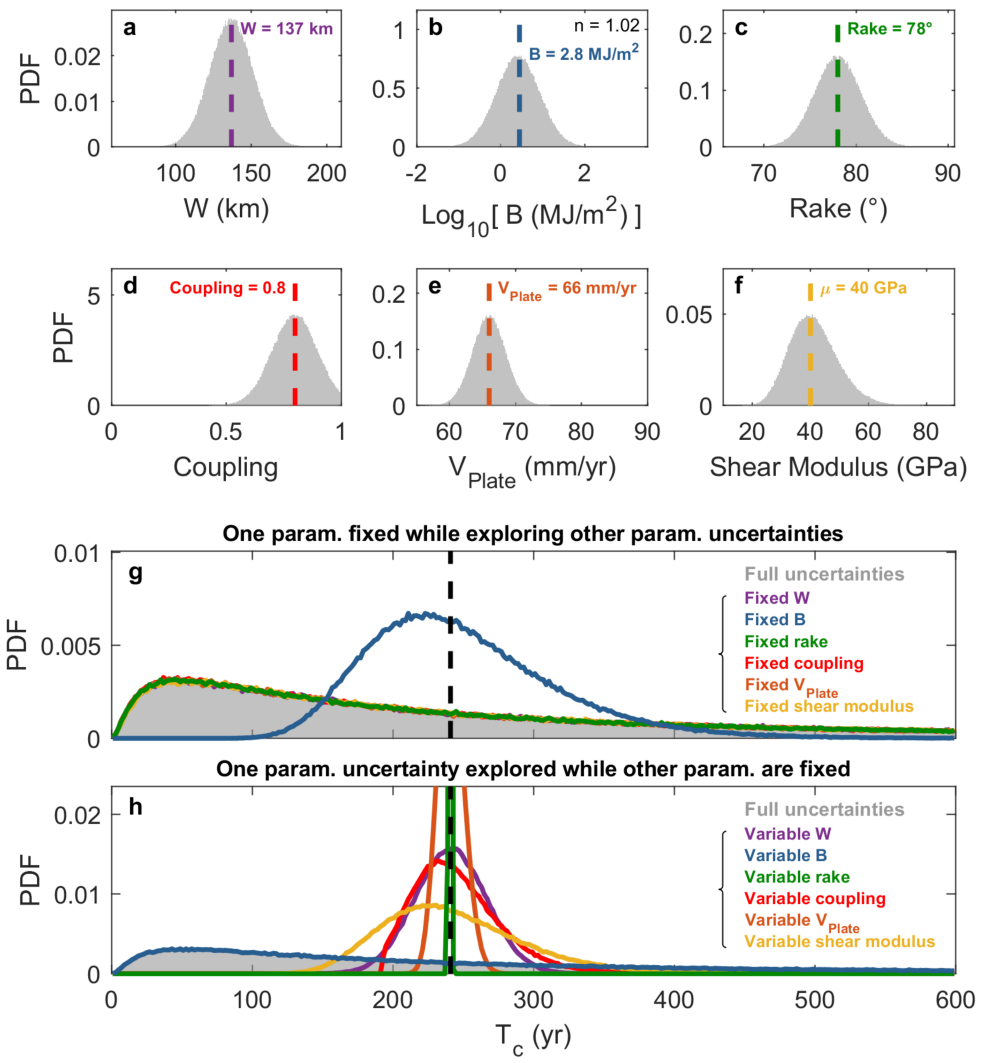

Fig. 2 Sensitivity of critical time T_c to uncertainties in model parameters. (a-f) PDF prescribed for each parameter, uniformly along strike. We draw randomly 300,000 combinations of parameters from these PDFs. **(g)** PDFs of T_c accounting for the uncertainties of all parameters but one. **(h)** PDFs of T_c accounting for the uncertainty of a single parameter. The colored vertical dashed lines in panels (a) to (f) indicate the fixed parameter values selected for the sensitivity tests. The gray histograms in (g) and (h) are the PDFs of T_c accounting for the uncertainties of all parameters.

323

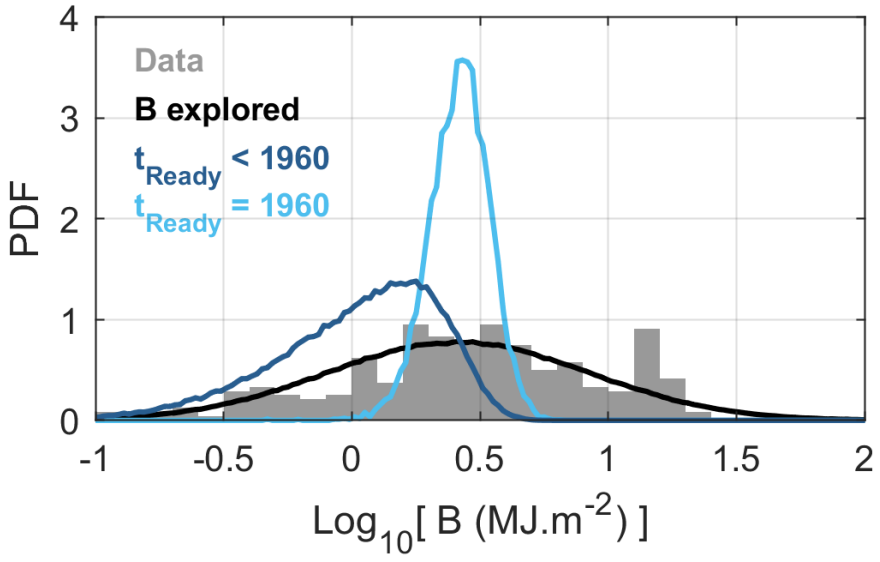

Fig. 3 Constraint on the fracture energy versus slip scaling coefficient B based on the Valdivia segment earthquake sequence. (Gray) empirical distribution of B based on estimates of G_c and D from seismological data compilation [33] (Fig. S1) and (black) its smooth approximation. Distribution of B according to different constraints: assuming the Valdivia segment is ready to host full-segment ruptures (dark blue) any time before the 1960 Mw 9.5 earthquake and (light blue) right in 1960.

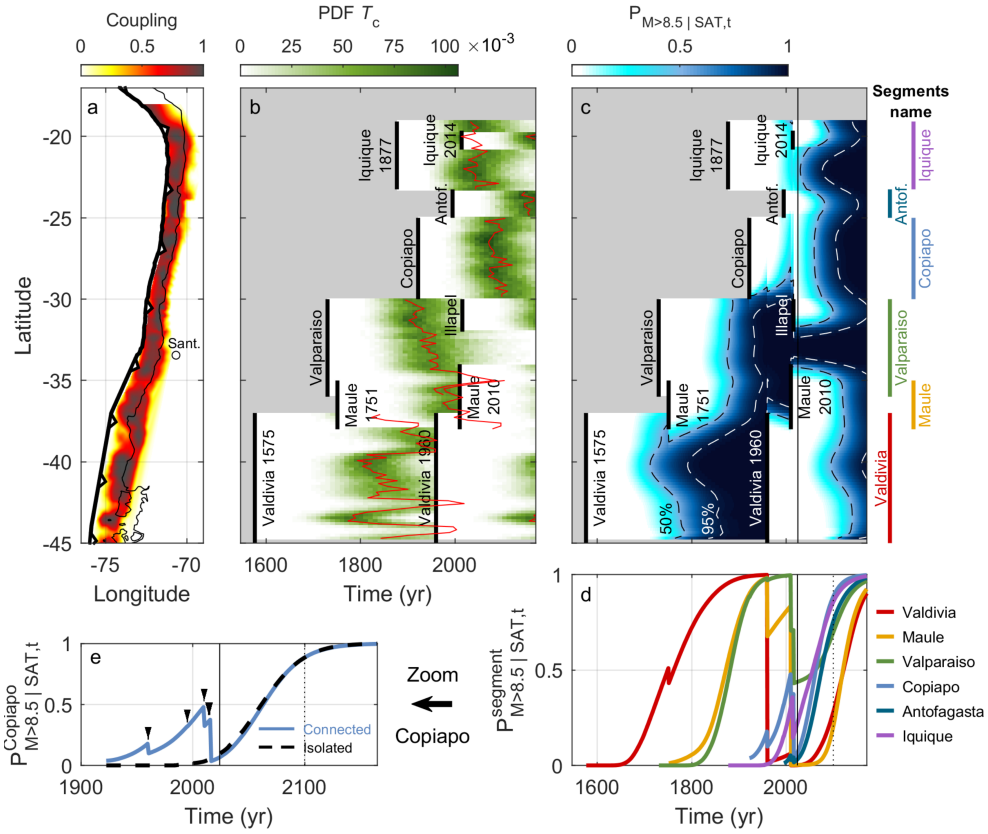

Fig. 4 Seismogenic potential of the Chilean subduction. **(a)** Coupling map of the Chilean subduction zone ([12, 20, 27–29]). The black thick and thin lines represent the trench and coast, respectively. The white dot indicates the city of Santiago. **(b)** PDF of critical time T_c (green color scale) and its mode (red curve) at each latitude. **(c)** Spatio-temporal evolution of $P_{M>8.5|SAT,t}$, the probability of a portion of the fault to host $M_w > 8.5$ events, knowing they already succeeded to saturate the seismogenic zone. The 50% and 95% iso-probabilities are indicated by the black and white dashed lines, respectively. The vertical thin black line indicates the year 2025. The gray shaded areas in panels (b) and (c) indicate the spatio-temporal zones that are not considered in the analysis, and where seismic events are not allowed to propagate. The colored vertical lines on the right of panel (c) indicates the extent of the segments considered. **(d)** Temporal evolution of the mean $P_{M>8.5|SAT,t}$ along each segment. **(e)** Zoom of the temporal evolution of mean $P_{M>8.5|SAT,t}$ of the Copiapo segment. The solid blue and dashed black lines correspond, respectively, to the scenarios where the Copiapó segment is fully connected to all other segments and completely isolated from them. The inverted black triangles indicate the occurrence of large earthquakes on neighboring segments. The vertical full and dashed black lines in panels (d) and (e) indicate the years 2025 and 2100, respectively.

325

7 Acknowledgment

This work was supported by the French government through the UCAJEDI Investments in the Future project (ANR-15-IDEX-01) managed by the National Research Agency (ANR). This project also received funding from the European Research Council (ERC) under the European Union's Horizon 2020 and Horizon Europe research and innovation programs (grant 758210 for project Geo4D and grant 101125232 for project iQuake). RJ acknowledges funding from the Institut Universitaire de France. AT acknowledges partial funding from FONDECYT project 1240862.

Methods

Determination of model parameters and their uncertainties

We present here the data used to evaluate the distributions of G_0 and G_c along the Chilean subduction zone.

The seismogenic width (W) of the Chilean megathrust is defined at any position along-strike as the along-dip distance between the trench location and the down-dip limit of shallow interplate thrust events in the instrumental seismicity record. From the CMT Harvard Catalog, we select the events consistent with slab interface faulting by applying two criteria: (1) a plunge of the tension axis larger than 45 degrees, corresponding to thrust events, and (2) depth between 20 km above and 25 km below the plate interface given by the Slab 2.0 model, to discard crustal thrust events while accounting for the vertical uncertainty of earthquake locations. In addition, for a more complete coverage of the entire margin, we consider focal mechanisms of small earthquakes, mainly on the Southern Andes [51]. The combined catalog contains 500 earthquakes. For each 0.6 degrees latitude bin, we define the down-dip limit of interplate seismicity by the location of the easternmost event. Based on the distance between this boundary and the trench (dt), we estimate the seismogenic width as

$W = dt/\cos(dip)$. We find a down-dip limit between 40 and 60 km depth, based on the pattern of seismicity and focal mechanisms ([52]; Fig. S4). We observe a lateral change at about 30°S (Fig. 1c): W is roughly 100 km north of this latitude and increases to 150 km to the south. These results agree well with previous estimates of W [53] and help explain why Chile hosted larger earthquakes in the south than in the north. We represent the uncertainties on W by a Gaussian distribution centered on the spatially smoothed version of W (Fig. 1c) with standard deviation of 14 km (i.e. the standard deviation of the difference between the rough and smoothed distributions of W). Smoothing is achieved by fitting a polynomial function of degree 3 to the W distribution along strike.

The plate rate V_{plate} and rake θ are assumed uniform along the whole subduction and their distributions are prescribed as follows. The PDF of V_{plate} is a Gaussian function with a mean and standard deviation equal to 66 $\pm$ 2.5 mm/yr, roughly the convergence rate between the Pacific and South American plates [e.g. 54, 55]. The PDF of θ is also taken as Gaussian with a mean and standard deviation of 78$\pm$ 2.5°, oblique to the subduction trench.

The distribution of coupling, χ, along strike is estimated by depth-averaging across the seismogenic width an interseismic coupling map compiled from various geodetic studies [20] (Fig. 1). We take trench-perpendicular profiles of χ spaced every 0.05 degrees, and calculate the average along each profile. Uncertainties on χ are described by a Gaussian distribution, with a mean value based on available coupling models (ref; Fig. 1c) and standard deviation of 0.1, truncated between 0 and 1.

The shear modulus μ is assumed constant over the whole subduction. Its PDF is described as a log-normal distribution with mean of 55 GPa and standard deviation of 8 GPa, from which we then subtract 14 GPa. This distribution increases at ~20 GPa, peaks at 40 GPa, and then decreases down to ~70 GPa. We set $\nu = 0.25$, and corresponding uncertainties are not explored. The geometric coefficient $C(\theta, \nu)$ is

estimated as [18]

$$C(\theta, \nu) = \frac{\pi}{4}\sqrt{(1-\nu)^2\cos^2\theta + \sin^2\theta} \tag{3}$$

For the sensitivity analysis and to constrain the fracture energy-slip scaling, we explore the uncertainties of the scaling law by fixing the exponent $n = 1.02$ and exploring the uncertainty of the prefactor B. The PDF of $Log_{10}[B]$ is set as a Gaussian distribution with mean 6.41 and standard deviation of 0.51, based on the spread of available seismological data [33] (Fig. S1).

For the sensitivity analysis, we evaluate the effect of parameter uncertainties on the critical time T_c for a given point on the fault. The uncertainties of the PDFs are prescribed as explained previously. We do not explore the effect of the spatial variability of parameters and consider a mean coupling of 0.8 and mean seismogenic width of 137 km, the mean values along the Chilean subduction. The PDF of each parameter is shown in Figs. 2a-f.

In Section *The seismogenic potential of the Chile subduction megathrust*, the parameters, including B, follow different distributions that are based on the constraint developed in Section *Constraining the scaling relation between fracture energy and slip* (Fig. S2).

Time and space-dependent evaluation of the seismogenic potential

We evaluate the seismogenic potential of a fault over time using the following procedure (Fig. S5). We discretize the fault along strike into a set of 20 km long subfaults, each spanning the whole seismogenic depth. At each time and for each possible hypocenter position along strike, we consider a set of ruptures that have initially saturated

the seismogenic width (initial length equal to initial width). We consider all possible positions of the saturating ruptures relative to the hypocenter. For each rupture, we determine its final extent using the theoretical arrest criterion (see Section *Determining the rupture extent of elongated earthquakes*; Figs. S5 and S6). The seismic moment of each earthquake is calculated as $M_0 = \int \mu D W dL$, integrated over its final rupture extent.

From the ensemble of scenarios, we can compute various probabilities, for instance the probability of an event exceeding a certain magnitude or breaking a whole segment or breaking through a barrier. Here, we focus on the probability at time t of a subfault to host earthquakes exceeding a certain magnitude, given that those earthquakes have already saturated the seismogenic zone, $P_{M>X|SAT,t}$. At any given time, we compute the probability $P_{M>X|SAT,t}$ that a fault location can participate in an event of magnitude exceeding X as the ratio, among the earthquake scenarios that rupture this fault location, between the number of events with $M > X$ and the total number of events.

The magnitude M_{SAT} above which our model's assumption of elongated ruptures is valid corresponds to the size at which earthquakes start to saturate the seismogenic zone. Here, we assume that such saturating earthquakes have a square rupture area, with length and width equal to the seismogenic width. Considering the range of seismogenic widths in Chile (thick purple line in Fig. 1c), from 104 to 153 km, and using an empirical moment-area scaling relationship for dip-slip earthquakes [38], we estimate that $M_{SAT} \approx$ 8.0-8.3.

The critical time T_c after which a fault section promotes rupture propagation instead of hindering it, derived from the condition $G_c/G_0 = 1$, is

$$T_c = \frac{1}{\chi V_{plate}} \left[\frac{\mu\, C(\theta,\nu) \left((1-\nu)^{-1} \cos^2\theta + \sin^2\theta \right)}{BW} \right]^{1/(n-2)} . \tag{4}$$

Determining the recurrence time of saturating events

To evaluate P_{SAT}, we propose two alternative approaches. In the first approach, for a given segment, we directly take the observed rate of $M_w \geq M_{SAT}$ events from the catalog, including events that started in other segments and propagated into the segment of interest. We further assume that their occurrence follows a Poisson process. In the second approach, we still assume that saturating events follow a Poisson process, but we match the rate of $M_w = M_{SAT}$ events predicted by our model with their observed rate. This approach requires a generative model of earthquakes, based on $P_{M>X \bigcap SAT}$, to extract the rate of $M_w = M_{SAT}$ events.

Discussion on the historical catalog

The quality of the historical catalog used has an impact on the results. The catalog selected for this study is a simplified one, a choice discussed here. As an example of the influence of the catalog, we provide estimates using a catalog that includes three additional events: the 1835 Maule, 1819 Copiapo and 1943 Illapel earthquakes (Fig. S7). With this catalog, $P_{M>X|SAT,t}$ on the Copiapo segment is close to 0 after the 1922 event because the 1943 Illapel earthquake has isolated the Copiapo segment from the energy available on the rest of the Valparaiso segment (Fig. S7c).

We assume that each event releases all the accumulated slip deficit. As a result, $P_{M>X|SAT,t}$ depends entirely on the most recent events that have occurred on each segment. After the 2015 Illapel earthquake, the evolution of $P_{M>X|SAT,t}$ is identical for both the initial and updated catalogs since both contain the same most recent earthquakes on each segment (Fig. S7c). If, instead, we allowed a residual slip deficit after each event, the evolution of $P_{M>X|SAT,t}$ after the 2015 Illapel earthquake might differ between the two catalogs.

The framework can also shed light on the interpretation of historical earthquakes. For example, it has been suggested that Copiapo's presumed-full-segment ruptures in

1819 and 1922 were actually due to multiple earthquakes [24]. Considering the short inter-event time between those two sequences, the model suggests that the fault did not have enough time to reload, which favors the interpretation of sequences of multiple ruptures rather than full-segment ruptures.

Finally, in our study, although along-strike heterogeneity in W and χ was explored, the parameter B was held constant over the whole subduction. In our model, this parameter quantifies the fault strength, which can be spatially heterogeneous. Incorporating additional constraints from observed earthquake sequences might help constrain along-strike variation in the naturally tunable parameter B, and improve the model's forecast capability.

References

[1] Corbi, F., Funiciello, F., Brizzi, S., Lallemand, S. & Rosenau, M. Control of asperities size and spacing on seismic behavior of subduction megathrusts. *Geophysical Research Letters* **44**, 8227–8235 (2017). doi: https://doi.org/10.1002/2017GL074182.

[2] Iacoletti, S., Cremen, G. & Galasso, C. Advancements in multi-rupture time-dependent seismic hazard modeling, including fault interaction. *Earth-Science Reviews* **220**, 103650 (2021). doi: https://doi.org/10.1016/j.earscirev.2021.103650.

[3] Stirling, M. *et al.* National seismic hazard model for new zealand: 2010 update. *Bulletin of the Seismological Society of America* **102**, 1514–1542 (2012). doi: https://doi.org/10.1785/0120110170.

[4] Pace, B., Visini, F. & Peruzza, L. Fish: Matlab tools to turn fault data into seismic-hazard models. *Seismological Research Letters* **87**, 374–386 (2016). doi: https://doi.org/10.1785/0220150189.

[5] Hagiwara, Y. Probability of earthquake occurrence as obtained from a weibull distribution analysis of crustal strain. *Tectonophysics* **23**, 313–318 (1974). doi: https://doi.org/10.1016/0040-1951(74)90030-4.

[6] Nishenko, S. P. & Buland, R. A generic recurrence interval distribution for earthquake forecasting. *Bulletin of the Seismological Society of America* **77**, 1382–1399 (1987). doi: https://doi.org/10.1785/BSSA0770041382.

[7] Matthews, M. V., Ellsworth, W. L. & Reasenberg, P. A. A brownian model for recurrent earthquakes. *Bulletin of the Seismological Society of America* **92**, 2233–2250 (2002). doi: https://doi.org/10.1785/0120010267.

[8] Field, E. H. Computing elastic-rebound-motivated earthquake probabilities in unsegmented fault models: A new methodology supported by physics-based simulators. *Bulletin of the Seismological Society of America* **105**, 544–559 (2015). doi: https://doi.org/10.1785/0120140094.

[9] Weng, H. & Ampuero, J.-P. The dynamics of elongated earthquake ruptures. *Journal of Geophysical Research: Solid Earth* **124**, 8584–8610 (2019). doi: https://doi.org/10.1029/2019JB017684.

[10] Chlieh, M. *et al.* Interseismic coupling and seismic potential along the central andes subduction zone. *Journal of Geophysical Research: Solid Earth* **116** (2011). doi: https://doi.org/10.1029/2010JB008166.

[11] Métois, M. *et al.* Revisiting the North Chile seismic gap segmentation using GPS-derived interseismic coupling. *Geophysical Journal International* **194**, 1283–1294 (2013). doi: https://doi.org/10.1093/gji/ggt183.

[12] Moreno, M., Rosenau, M. & Oncken, O. 2010 maule earthquake slip correlates with pre-seismic locking of andean subduction zone. *Nature* **467**, 198–202 (2010).

[13] Loveless, J. P. & Meade, B. J. Spatial correlation of interseismic coupling and coseismic rupture extent of the 2011 mw = 9.0 tohoku-oki earthquake. *Geophysical Research Letters* **38** (2011). doi: https://doi.org/10.1029/2011GL048561.

[14] Milner, K. R. *et al.* Appendix t—defining the inversion rupture set using plausibility filters. *US Geol. Surv. Open-File Rept. 2013-1165* (2013).

[15] Parsons, T., Field, E. H., Page, M. T. & Milner, K. Possible earthquake rupture connections on mapped california faults ranked by calculated coulomb linking stresses. *Bulletin of the Seismological Society of America* **102**, 2667–2676 (2012). doi: https://doi.org/10.1785/0120110349.

[16] Murray, J. & Segall, P. Testing time-predictable earthquake recurrence by direct measurement of strain accumulation and release. *Nature* **419**, 287–291 (2002). doi: https://doi.org/10.1038/nature00984.

[17] Shaw, B. E., Milner, K. R. & Goulet, C. A. Deterministic physics-based earthquake sequence simulators match empirical ground-motion models and enable extrapolation to data-poor regimes: Application to multi-fault multimechanism ruptures. *Seismological Research Letters* (2025). doi: https://doi.org/10.1785/0220240141.

[18] Weng, H. & Ampuero, J.-P. Continuum of earthquake rupture speeds enabled by oblique slip. *Nature Geoscience* **13**, 817–821 (2020). doi: https://doi.org/10.1038/s41561-020-00654-4.

[19] Diao, F., Weng, H., Shao, Z., Wang, R. & Xiong, X. Physics-based assessment of earthquake potential on the anninghe-zemuhe fault system in southwestern china. *Nature Communications* **15** (2024). doi: https://doi.org/10.1038/s41467-024-51313-w.

[20] Molina, D., Tassara, A., Abarca, R., Melnick, D. & Madella, A. Frictional segmentation of the chilean megathrust from a multivariate analysis of geophysical, geological, and geodetic data. *Journal of Geophysical Research: Solid Earth* **126**, e2020JB020647 (2021).

[21] Comte, D. & Pardo, M. Reappraisal of great historical earthquakes in the northern chile and southern peru seismic gaps. *Natural hazards* **4**, 23–44 (1991). doi: https://doi.org/10.1007/BF00126557.

[22] Ruiz, S. & Madariaga, R. Historical and recent large megathrust earthquakes in chile. *Tectonophysics* **733**, 37–56 (2018). doi: https://doi.org/10.1016/j.tecto.2018.01.015.

[23] Vigny, C. & Klein, E. The 1877 megathrust earthquake of north chile two times smaller than thought? a review of ancient articles. *Journal of South American Earth Sciences* **117**, 103878 (2022). doi: https://doi.org/10.1016/j.jsames.2022.103878.

[24] Vigny, C., Klein, E. & Ojeda, J. In search for the lost truth about the 1922 & 1918 atacama earthquakes in chile. *Journal of South American Earth Sciences* **143**, 104983 (2024). doi: https://doi.org/10.1016/j.jsames.2024.104983.

[25] Cisternas, M. *et al.* Predecessors of the giant 1960 chile earthquake. *Nature* **437**, 404–407 (2005). doi: https://doi.org/10.1038/nature039434.

[26] Salazar, D. *et al.* Did a 3800-year-old ¡i¿m¡/i¿¡sub¿w¡/sub¿ 9.5 earthquake trigger major social disruption in the atacama desert? *Science Advances* **8**, eabm2996 (2022). doi: https://doi.org/10.1126/sciadv.abm2996.

[27] Moreno, M. *et al.* Toward understanding tectonic control on the mw 8.8 2010 maule chile earthquake. *Earth and Planetary Science Letters* **321**, 152–165

(2012). doi: https://doi.org/10.1016/j.epsl.2012.01.006.

[28] Li, S., Moreno, M., Bedford, J., Rosenau, M. & Oncken, O. Revisiting viscoelastic effects on interseismic deformation and locking degree: A case study of the peru-north chile subduction zone. *Journal of Geophysical Research: Solid Earth* **120**, 4522–4538 (2015). doi: https://doi.org/10.1002/2015JB011903.

[29] Tilmann, F. *et al.* The 2015 illapel earthquake, central chile: A type case for a characteristic earthquake? *Geophysical Research Letters* **43**, 574–583 (2016). doi: https://doi.org/10.1002/2015GL066963.

[30] Sippl, C., Moreno, M. & Benavente, R. Microseismicity appears to outline highly coupled regions on the central chile megathrust. *Journal of Geophysical Research: Solid Earth* **126**, e2021JB022252 (2021). doi: https://doi.org/10.1029/2021JB022252.

[31] González-Vidal, D. *et al.* Relation Between Oceanic Plate Structure, Patterns of Interplate Locking and Microseismicity in the 1922 Atacama Seismic Gap. *Geophysical Research Letters* **50**, e2023GL103565 (2023). doi: https://doi.org/10.1029/2023GL103565.

[32] Michel, S., Jolivet, R., Jara, J. & Rollins, C. Seismogenic Potential of the Subduction Zone in Northern Chile. *Bulletin of the Seismological Society of America* **113**, 1013–1024 (2023). doi: https://doi.org/10.1785/0120220142.

[33] Cocco, M. *et al.* Fracture energy and breakdown work during earthquakes. *Annual Review of Earth and Planetary Sciences* **51**, 217–252 (2023). doi: https://doi.org/10.1146/annurev-earth-071822-100304.

[34] Andrews, D. Rupture dynamics with energy loss outside the slip zone. *Journal of Geophysical Research: Solid Earth* **110** (2005). doi:

https://doi.org/10.1029/2004JB003191.

[35] Gabriel, A.-A., Ampuero, J.-P., Dalguer, L. & Mai, P. M. Source properties of dynamic rupture pulses with off-fault plasticity. *Journal of Geophysical Research: Solid Earth* **118**, 4117–4126 (2013). doi: https://doi.org/10.1002/jgrb.50213.

[36] Moernaut, J. *et al.* Larger earthquakes recur more periodically: New insights in the megathrust earthquake cycle from lacustrine turbidite records in south-central chile. *Earth and Planetary Science Letters* **481**, 9–19 (2018). doi: https://doi.org/10.1016/j.epsl.2017.10.016.

[37] Moreno, M. S., Bolte, J., Klotz, J. & Melnick, D. Impact of megathrust geometry on inversion of coseismic slip from geodetic data: Application to the 1960 chile earthquake. *Geophysical Research Letters* **36** (2009). doi: https://doi.org/10.1029/2009GL039276.

[38] Leonard, M. Earthquake fault scaling: Self-consistent relating of rupture length, width, average displacement, and moment release. *Bulletin of the Seismological Society of America* **100**, 1971–1988 (2010). doi: https://doi.org/10.1785/0120090189.

[39] Rong, Y., Jackson, D. D., Magistrale, H. & Goldfinger, C. Magnitude limits of subduction zone earthquakes. *Bulletin of the Seismological Society of America* **104**, 2359–2377 (2014). doi: https://doi.org/10.1785/0120130287.

[40] Johnson, K., Pagani, M. & Styron, R. Psha of the southern pacific islands. *Geophysical Journal International* **224**, 2149–2172 (2021). doi: https://doi.org/10.1093/gji/ggaa530.

[41] Melnick, D. *et al.* The super-interseismic phase of the megathrust earthquake cycle in chile. *Geophysical Research Letters* **44**, 784–791 (2017). doi:

https://doi.org/10.1002/2016GL071845.

[42] Jara, J., Jolivet, R., Socquet, A., Comte, D. & Norabuena, E. Detection of slow slip events along the southern peru-northern chile subduction zone. *Seismica* **3** (2024). doi: https://doi.org/10.26443/seismica.v3i1.980.

[43] Klein, E. *et al.* Return of the atacama deep slow slip event: The 5-year recurrence confirmed by continuous gps. *Physics of the Earth and Planetary Interiors* **334**, 106970 (2023). doi: https://doi.org/10.1016/j.pepi.2022.106970.

[44] Molina-Ormazabal, D. *et al.* Slip modes along a structurally-driven earthquake barrier in chile. *Journal of Geophysical Research: Solid Earth* **130**, e2024JB030796 (2025). doi: https://doi.org/10.1029/2024JB030796.

[45] Nocquet, J.-M. *et al.* Supercycle at the ecuadorian subduction zone revealed after the 2016 pedernales earthquake. *Nature Geoscience* **10**, 145–149 (2017). doi: https://doi.org/10.1038/ngeo2864.

[46] Kaneko, Y., Avouac, J.-P. & Lapusta, N. Towards inferring earthquake patterns from geodetic observations of interseismic coupling. *Nature Geoscience* **3**, 363–369 (2010). doi: https://doi.org/10.1038/ngeo843.

[47] Michel, S., Jolivet, R., Rollins, C., Jara, J. & Dal Zilio, L. Seismogenic potential of the main himalayan thrust constrained by coupling segmentation and earthquake scaling. *Geophysical Research Letters* **48**, e2021GL093106 (2021). doi: https://doi.org/10.1029/2021GL093106.

[48] Ozawa, S., Ando, R. & Dunham, E. M. Quantifying the probability of rupture arrest at restraining and releasing bends using earthquake sequence simulations. *Earth and Planetary Science Letters* **617**, 118276 (2023). doi: https://doi.org/10.1016/j.epsl.2023.118276.

[49] Molina-Ormazabal, D., Ampuero, J.-P. & Tassara, A. Diverse slip behaviour of velocity-weakening fault barriers. *Nature Geoscience* **16**, 1200–1207 (2023). doi: https://doi.org/10.1038/s41561-023-01312-1.

[50] Weng, H. & Ampuero, J.-P. Integrated rupture mechanics for slow slip events and earthquakes. *Nature Communications* **13**, 7327 (2022). doi: https://doi.org/10.1038/s41467-022-34927-w.

[51] Herrera, C., Cassidy, J. F., Dosso, S. E., Bastías, N. & Onur, T. Ground-motion evaluation of moderate and large interface earthquakes along the chilean subduction zone. *Bulletin of the Seismological Society of America* **110**, 2693–2710 (2020). doi: https://doi.org/10.1785/0120190265.

[52] del Rosario Martínez-López, M., Mendoza, C. & Mendoza, A. I. Seismogenic width in the guerrero-oaxaca subduction zone of mexico. *Journal of South American Earth Sciences* **117**, 103885 (2022). doi: https://doi.org/10.1016/j.jsames.2022.103885.

[53] Herrendörfer, R., van Dinther, Y., Gerya, T. & Dalguer, L. A. Earthquake supercycle in subduction zones controlled by the width of the seismogenic zone. *Nature Geoscience* **8**, 471–474 (2015). doi: https://doi.org/10.1038/ngeo2427.

[54] Argus, D. F., Gordon, R. G. & DeMets, C. Geologically current motion of 56 plates relative to the no-net-rotation reference frame. *Geochemistry, Geophysics, Geosystems* **12** (2011). doi: https://doi.org/10.1029/2011GC003751.

[55] Vigny, C. *et al.* Upper plate deformation measured by gps in the coquimbo gap, chile. *Physics of the Earth and Planetary Interiors* **175**, 86–95 (2009). doi: https://doi.org/10.1016/j.pepi.2008.02.013.

[56] Carvajal, M. *et al.* Large size of two 19th-century chile-peru earthquakes inferred from trans-pacific tsunami records. *Geophysical Research Letters* **52**, e2024GL113849 (2025). doi: https://doi.org/10.1029/2024GL113849.

Supplementary Information

Time-dependent forecast of large earthquakes from physics-informed probabilistic approach

Text S1 Comparison between forecast and observed magnitudes

Here, we compare the forecast of the magnitude of past events with their observed values in the original catalog (Fig. S8) and in the updated catalog (Fig. S9). The magnitude forecast for the Valdivia 1960 earthquake is slightly lower than the observed one. This discrepancy can be partly explained by a maximum slip deficit of ∼25 m accumulated between the 1575 and 1960 events (assuming a loading rate of 66 mm/yr), which is further decreased when accounting for coupling (Fig. 1c), and therefore does not reach the observed 20-35 m slip of the 1960 event. For the 2010 Maule earthquake, the magnitude probability is multimodal, with the two largest peaks located at M_w ∼8.6 and 9.1 based on the original catalog. The latter corresponds to scenarios in which the event rupture extends to the Valparaiso segment. The model forecasts a M_w ∼8.9 for the 2015 Illapel earthquake which was actually a M_w ∼8.3 event. This overestimation arises because, in the original catalog, no earthquakes are recorded between the 1730 Valparaiso event and 2015, resulting in a large accumulated slip deficit. Moreover, most of the forecast ruptures involve the rest of the Valparaiso segment. The inclusion of the 1943 event in the updated catalog (Fig. S7) helps correct this overestimation to some extent (Fig. S9). Finally, the 2014 Iquique earthquake, along with its main aftershock, falls within the forecast magnitudes, although some debate remains about the overlap between the 1877 and 2014 events [23, 56]. When additional earthquakes are incorporated - as in the updated catalog - the forecast magnitudes change because each added event resets the available elastic energy within its rupture extent and can isolate certain segments from available elastic energy on neighboring segments.

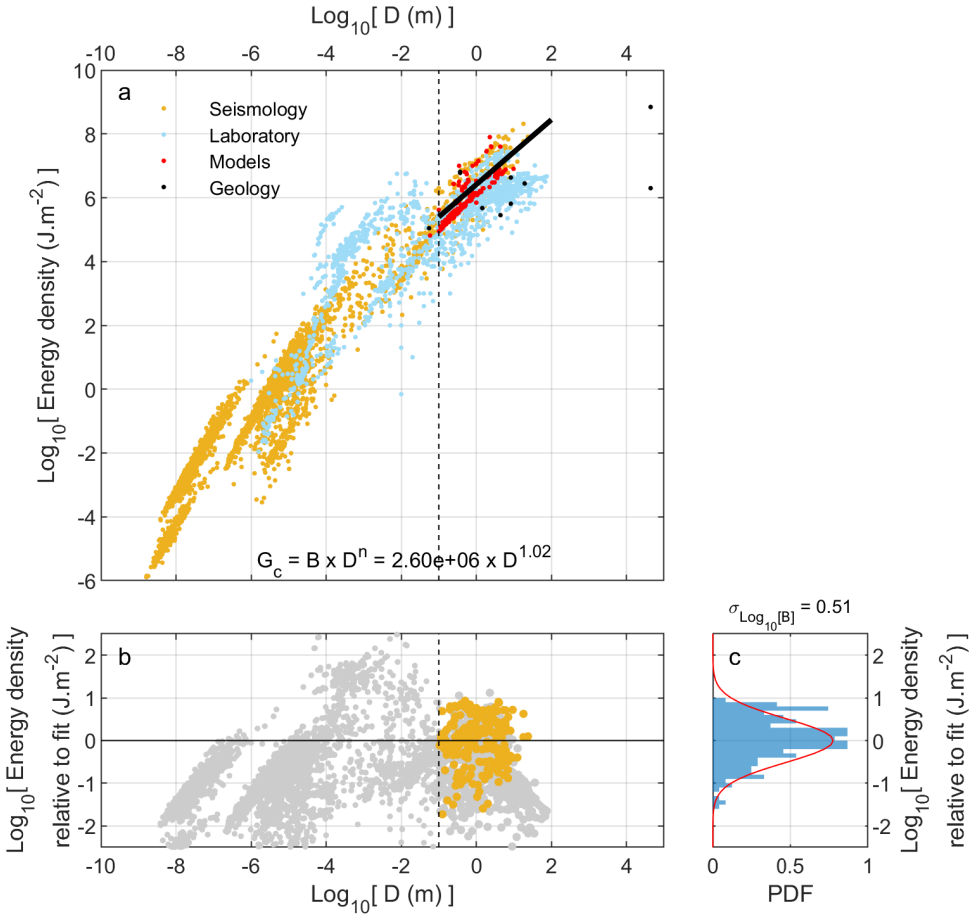

Fig. S1 Scaling relation between fracture energy and final slip. **(a)** Estimates of fracture energy, G_c, and earthquake slip, D, compiled by [33]. Colors indicate different types of G_c estimates. Solid black line: best-fitting scaling relation (power law equation at the bottom) for D >0.1 m (vertical black dashed line) using only seismological data (yellow dots). **(b)** Residuals between G_c estimates and the best-fitting scaling relation. Gray and yellow dots represent the data that are disregarded and used, respectively, to determine the scaling relation. **(c)** Histogram of the residuals (blue) and a Gaussian approximation to it (red, with a standard deviation of 0.51 $Log_{10}[J.m^{-2}]$) used in this study to represent the uncertainty of B.

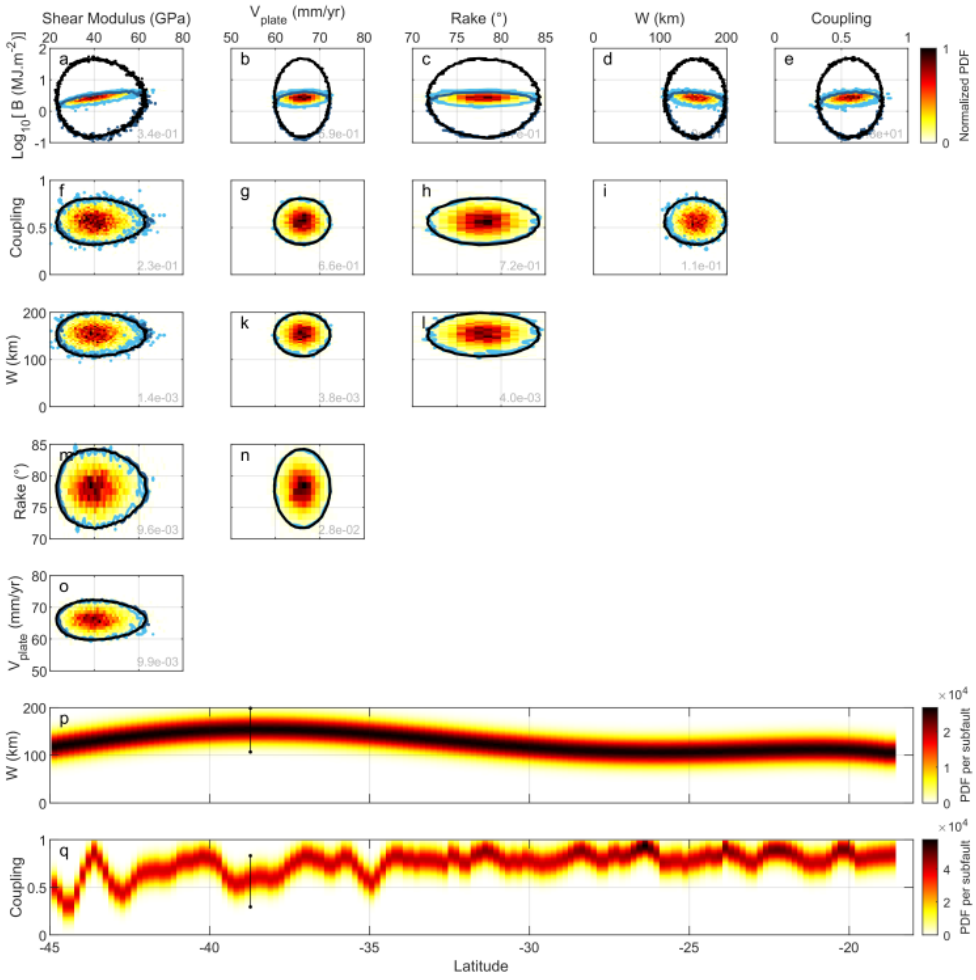

Fig. S2 Constraints on model parameters based on the Valdivia segment's inter-event time. **(a)-(o)** Normalized PDFs of each model parameter, constrained by the assumption that the 1960 M9.5 Valdivia earthquake occurs immediately after the whole southern portion of the Valdivia segment (south of latitude 38°S) is ready to rupture (Section 4). Maximum value of the PDFs are indicated in gray at the bottom right of each panel. Contours of 5% of the maximum PDF value are shown for different constraints imposed: (black) initial parameter distribution described in the Method section Determination of model parameters and their uncertainties, parameter distribution assuming the portion of the Valdivia segment south of latitude 38°S is ready to rupture fully (dark blue) any time before the 1960 earthquake and (light blue) exactly at the occurrence time of the 1960 earthquake. The distributions of W and coupling are taken from a location on the fault shown by the vertical black line in panels (p) and (q). **(p)** PDF of the seismogenic width W for each subfault. **(q)** PDF of the interseismic coupling for each subfault.

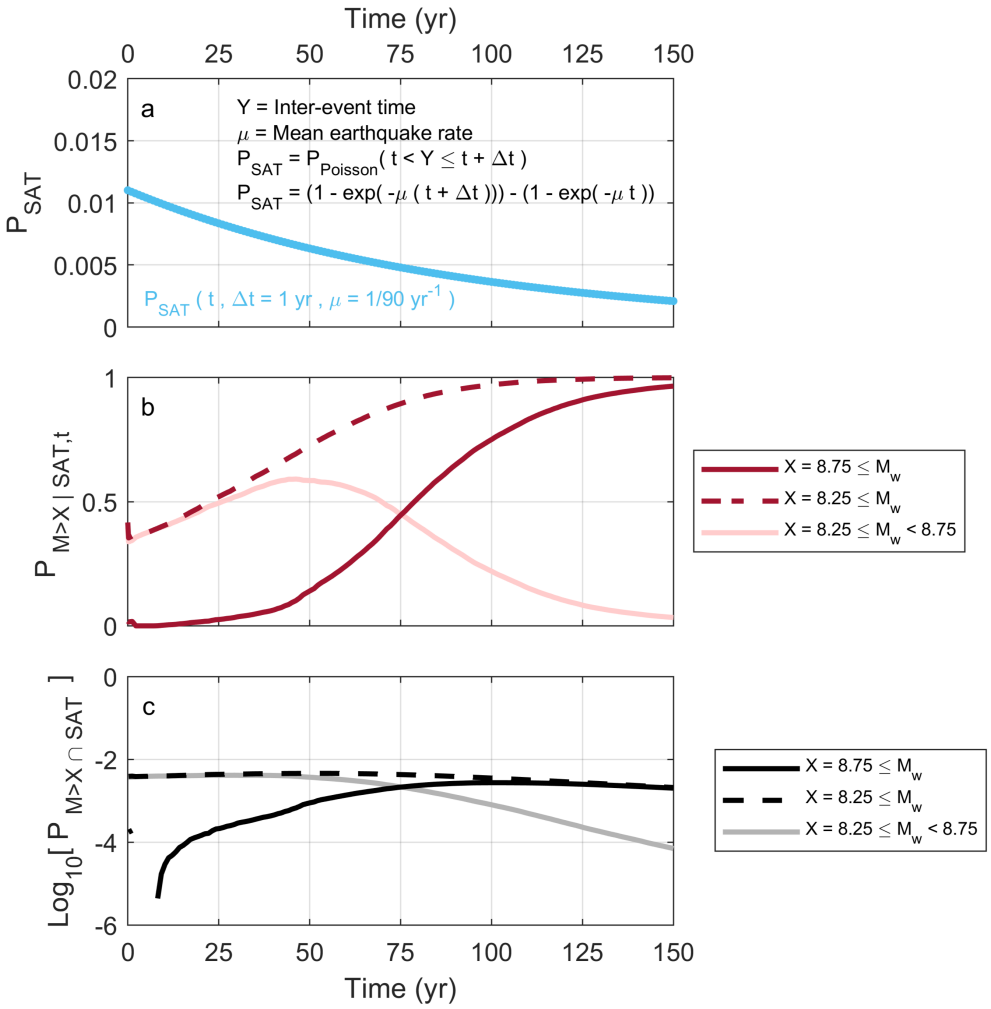

Fig. S3 Evaluation of the probability of an earthquake to saturate the seismogenic zone and to reach a certain magnitude. **(a)** Probability of the inter-event time of saturating earthquakes, P_{SAT}, assuming their occurrence follows a Poisson process with a mean rate of $\mu = 1/90$ yrs^{-1}. **(b)** Probability $P_{M>X|SAT,t}$ that an earthquake will exceed magnitude X given that its rupture has already saturated the seismogenic width at time t. We show here the case for the Iquique and Antofagasta segments combined, with $t = 0$ corresponding to the occurrence of the 2014 Iquique earthquake. **(c)** Probability of occurrence of an earthquake exceeding magnitude X within an interval of 1 year around time t, $P_{M>X \bigcap SAT} = P_{M>X|SAT,t} \times P_{SAT}$.

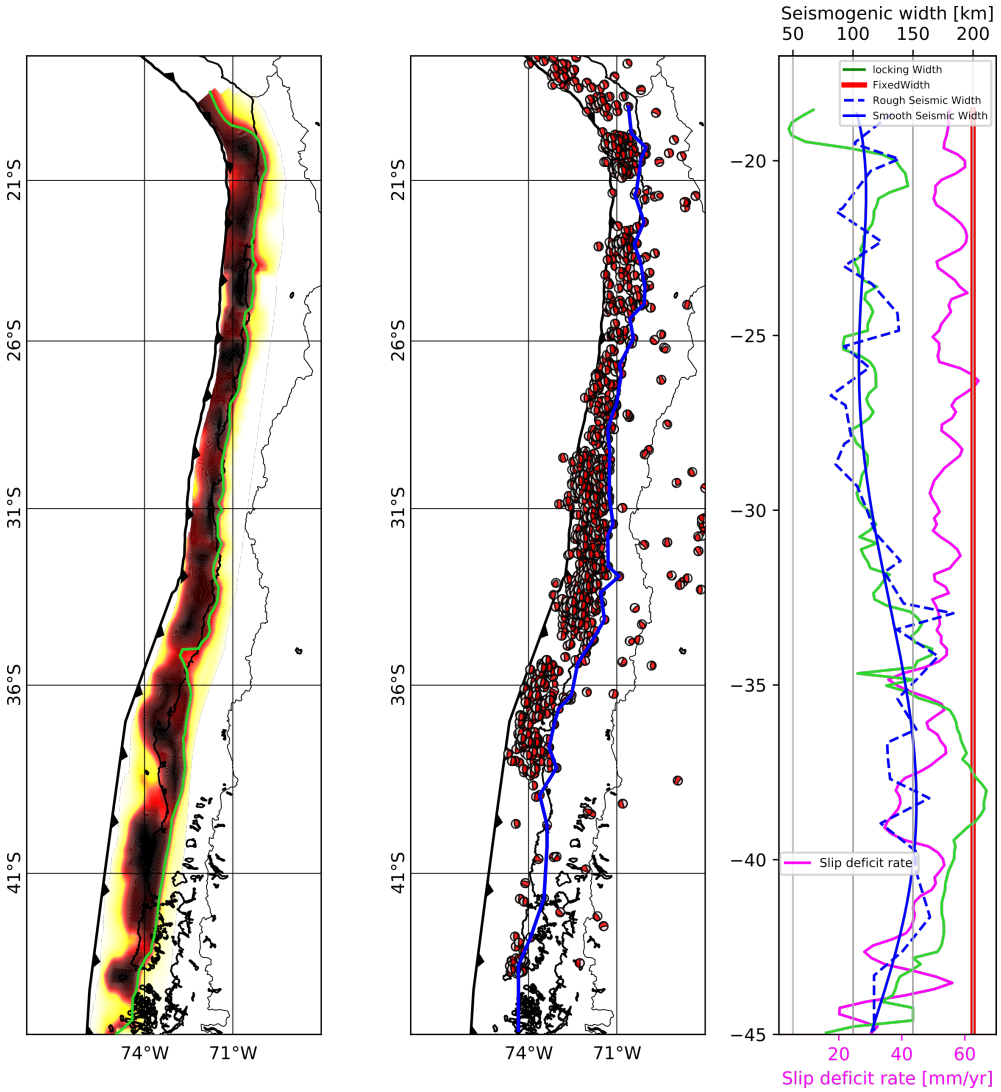

Fig. S4 **(a)** Interseismic coupling along the Chilean subduction megathrust [12, 20, 27–29]. **(b)** Focal mechanisms of earthquakes in Chile from 1980 to 2022 [52], used to estimate the seismogenic depth. **(c)** Comparison between seismogenic widths estimated from interseismic coupling and seismicity.

Fig. S5 Cartoon illustrating the different earthquake scenarios tested to evaluate the seismogenic potential at a time t.

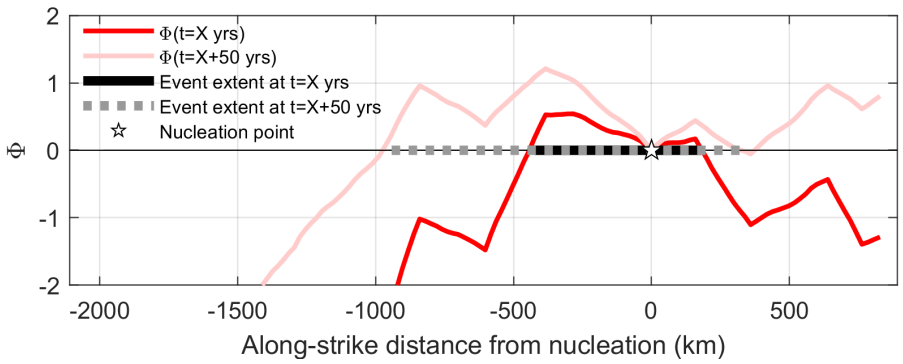

Fig. S6 Example of distribution of rupture potential Φ for a specific earthquake scenario (see Fig. S5) and at two different times. The white star indicates the hypocenter location tested, which is also used here as reference point for Φ without loss of generality. At time X, the earthquake propagates until Φ (red curve) passes below its hypocentral value; its final rupture extent is indicated by the thick horizontal black line. At time $X + 50$ yrs, the fault has been loaded further, thus modifying Φ (pink curves). The earthquake can now propagate further, as indicated by the thick dotted gray line.

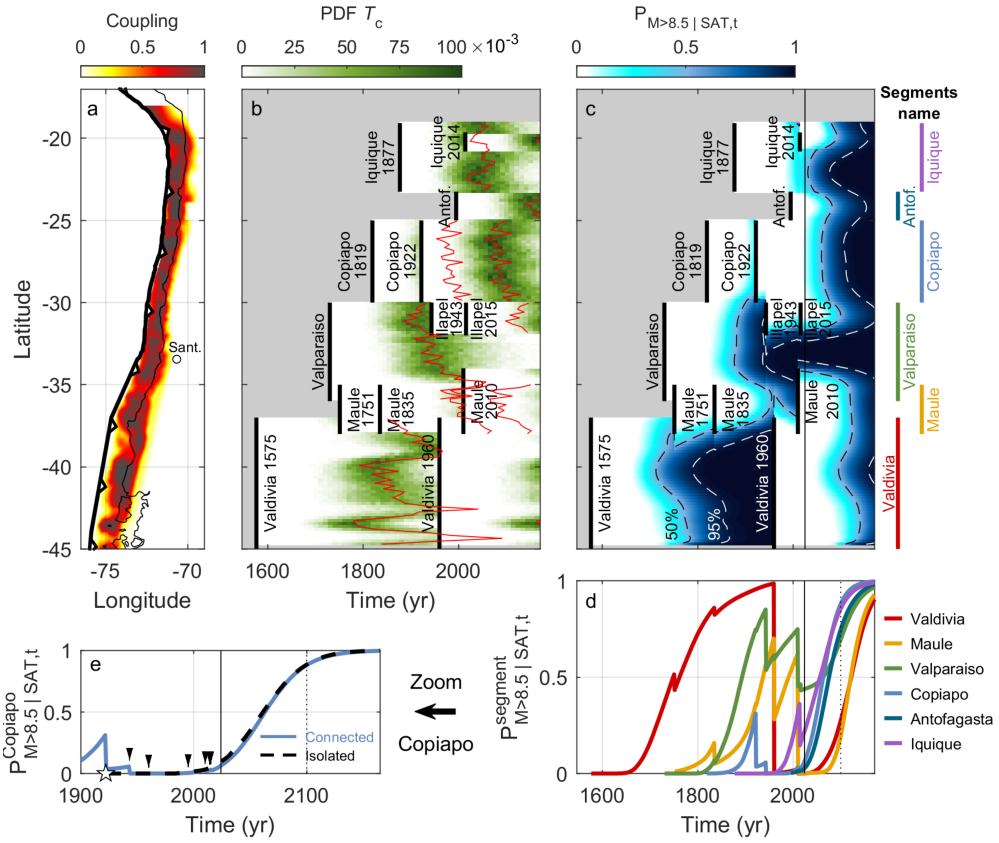

Fig. S7 Same as Fig. 4 but using an alternative historical earthquake catalog that includes the 1819 Copiapo, 1943 Illapel and 1835 Maule earthquakes. The white star in panel (e) indicates the timing of the 1922 earthquake on the Copiapo segment.

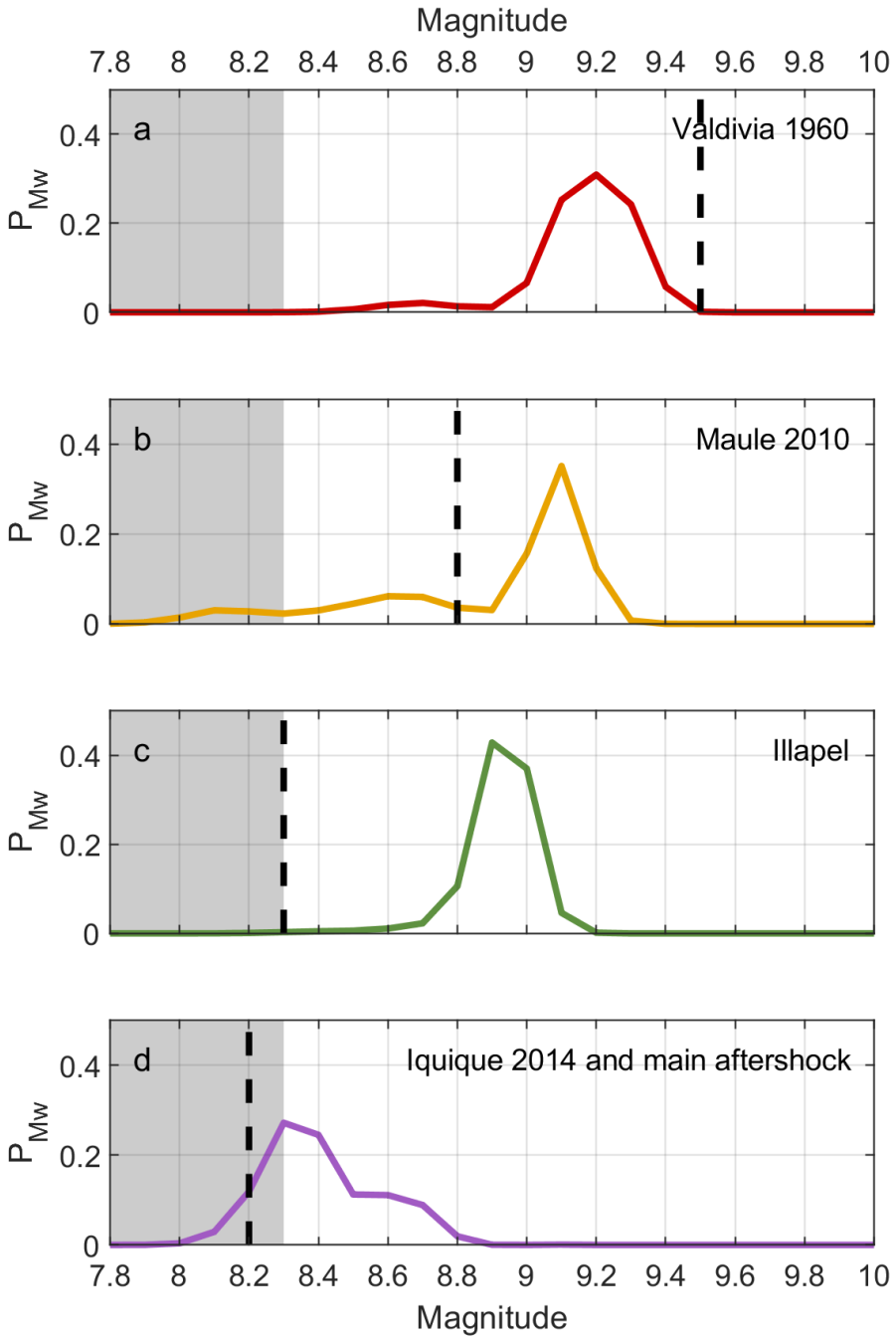

Fig. S8 Forecast of earthquake magnitude at the location and time of known events. The vertical black dashed line indicates the observed magnitude. The gray-shaded area represents a magnitude range that should not be interpreted, as events within those magnitudes are unlikely to saturate the seismogenic zone. Curve colors correspond to the segments shown in Fig. 4.

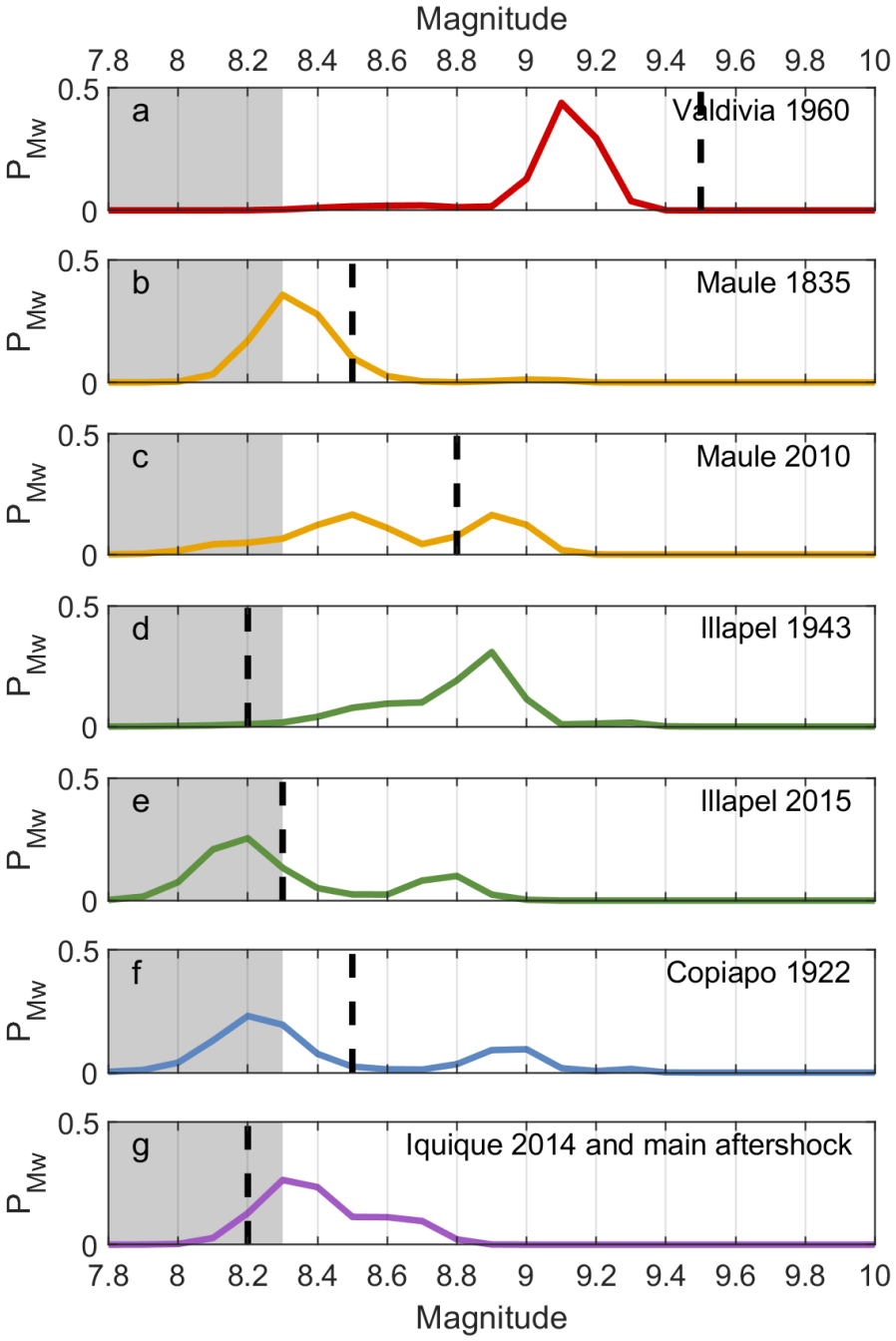

Fig. S9 Same as Fig. S8, but for the updated catalog (Fig. S7).